

# Transport Effects on Multiple-Component Reactions in Optical Biosensors

Ryan M. Evans<sup>1</sup> · David A. Edwards<sup>2</sup>

Received: 20 October 2016 / Accepted: 20 July 2017 / Published online: 1 August 2017  
© Society for Mathematical Biology (outside the USA) 2017

**Abstract** Optical biosensors are often used to measure kinetic rate constants associated with chemical reactions. Such instruments operate in the *surface–volume* configuration, in which ligand molecules are convected through a fluid-filled volume over a surface to which receptors are confined. Currently, scientists are using optical biosensors to measure the kinetic rate constants associated with DNA translesion synthesis—a process critical to DNA damage repair. Biosensor experiments to study this process involve multiple interacting components on the sensor surface. This multiple-component biosensor experiment is modeled with a set of nonlinear integrodifferential equations (IDEs). It is shown that in physically relevant asymptotic limits these equations reduce to a much simpler set of ordinary differential equations (ODEs). To verify the validity of our ODE approximation, a numerical method for the IDE system is developed and studied. Results from the ODE model agree with simulations of the IDE model, rendering our ODE model useful for parameter estimation.

**Keywords** Biochemistry · Optical biosensors · Rate constants · Integrodifferential equations · Numerical methods

---

This work was done with the support of the National Science Foundation under Award Number NSF-DMS 1312529. The first author was also partially supported by the National Research Council through an NRC postdoctoral fellowship.

---

✉ Ryan M. Evans  
ryan.evans@nist.gov

David A. Edwards  
dedwards@udel.edu

<sup>1</sup> Applied and Computational Mathematics Division, Information and Technology Laboratory, National Institute of Standards and Technology, Gaithersburg, MD 20899, USA

<sup>2</sup> Department of Mathematical Sciences, University of Delaware, Newark, DE 19716, USA

## 1 Introduction

Kinetic rate constants associated with chemical reactions are often measured using optical biosensors. Such instruments operate in the *surface–volume* configuration in which ligand molecules are convected through a fluid-filled volume, over a surface to which receptors are immobilized. Ligand molecules are transported through the fluid onto the surface to bind with available receptor sites, creating bound ligand molecules at concentration  $B(x, t)$ . Mass changes on the surface due to ligand binding are averaged over a portion of the channel floor  $[x_{\min}, x_{\max}]$  to produce measurements of the form

$$\bar{B}(t) = \frac{1}{x_{\max} - x_{\min}} \int_{x_{\min}}^{x_{\max}} B(x, t) dx. \quad (1)$$

See Fig. 1 for a schematic of one such biosensor experiment.

Measuring kinetic rate constants with optical biosensors requires an accurate model of this process, and models have been successfully proposed and progressively refined throughout the years: Edwards (1999, 2000, 2001, 2006, 2011), Edwards et al. (1999), Lebedev et al. (2006) and Zumburum and Edwards (2014, 2015). Although such models are typically limited to reactions involving only a single molecule or a single step, chemists are currently using biosensor technology to measure rate constants associated with reactions involving multiple interacting components. In particular, chemists are now using biosensor experiments to elucidate how cells cope with DNA damage.

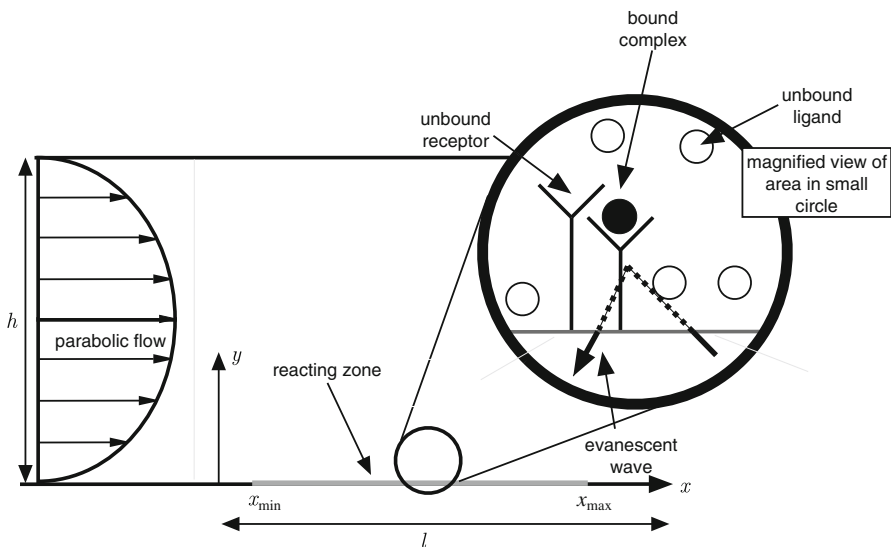


**Fig. 1** Cross-sectional schematic of an optical biosensor experiment. The instrument has length  $l$  and height  $h$ ; for instrument dimensions see Appendix. The origin corresponds to the lower left-hand corner of the instrument. Ligand molecules are convected into instrument at  $x = 0$  in a Poiseuille flow profile and transported to the surface to bind with receptors immobilized on reacting zone of the channel floor  $[x_{\min}, x_{\max}]$

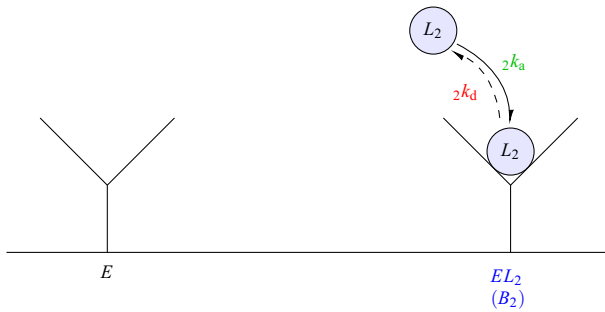


**Fig. 2** (Color figure online) *Left* an empty receptor  $E$ . *Right* direct binding of  $L_2$  with an empty receptor  $E$ . This creates the product  $EL_2$ . The function  $B_2$  is the concentration of  $EL_2$

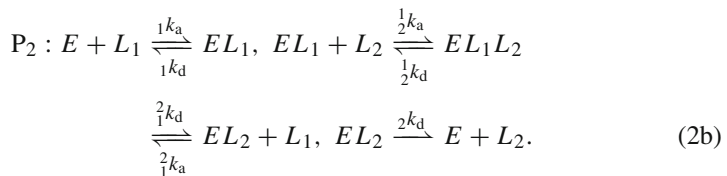
Harmful DNA lesions can impair a cell’s ability to replicate DNA and its ability to survive. One way a cell may respond to a DNA lesion is through DNA translesion synthesis (Friedberg 2005; Lehmann et al. 2007; Plosky and Woodgate 2004). For a description of this process, we refer the interested reader to the references included herein; however, for our purposes it is sufficient to know that DNA translesion synthesis involves three interacting components: a proliferating cell nuclear antigen (PCNA) molecule, polymerase  $\delta$ , and polymerase  $\eta$ . Moreover, in order for a successful DNA translesion synthesis event to occur polymerase  $\eta$  must bind with the PCNA molecule. A central question surrounding DNA translesion synthesis is whether the polymerase  $\eta$  and PCNA complex forms through direct binding or through a catalysis-type *ligand switching process* (Zhuang et al. 2008).

The former scenario is depicted in Fig. 2, where we have shown polymerase  $\eta$  directly binding with a PCNA molecule, i.e., the reaction:



Here, we have denoted the PCNA molecule and polymerase  $\eta$  as  $E$  and  $L_2$ , respectively. Additionally,  $2k_a$  denotes the rate at which  $L_2$  binds with an empty receptor  $E$ , and  $2k_d$  denotes the rate at which  $L_2$  dissociates from a receptor  $E$ . We will refer to this as pathway one, or simply  $P_1$  as in (2a).

The catalysis-type ligand switching process is depicted in Fig. 3 and stated precisely as:



In (2b) and Fig. 3 we have denoted polymerase  $\delta$  as  $L_1$ . This process is summarized as follows: First,  $L_1$  binds with an available receptor  $E$ ; next,  $L_2$  associates with  $EL_1$

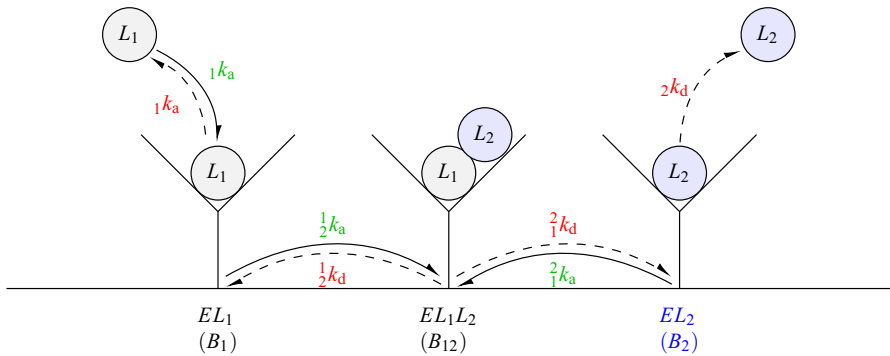


**Fig. 3** (Color figure online) Schematic of the ligand switching process. First,  $L_1$  binds with an available receptor  $E$ ; next,  $L_2$  associates with  $EL_1$  to create the product  $EL_1L_2$ ; then,  $L_1$  dissociates from the complex  $EL_1L_2$  to leave  $EL_2$ ; finally,  $L_2$  dissociates from  $EL_2$ . Below each of the species  $EL_1$ ,  $EL_1L_2$ , and  $EL_2$ , we have listed their corresponding concentrations  $B_1$ ,  $B_{12}$ , and  $B_2$

to create the product  $EL_1L_2$ ; then,  $L_1$  dissociates from  $EL_1L_2$ , leaving  $EL_2$ ; finally,  $L_2$  dissociates from  $EL_2$ . Furthermore, in (2b) and Fig. 3 the rate constants  ${}_1k_a$  and  ${}_1k_d$  denote the rates at which  $L_1$  binds and unbinds with a receptor  $E$ ,  ${}^j_kk_a$  denotes the rate at which ligand  $L_i$  binds with the product  $EL_j$ , and  ${}^j_kk_d$  denotes the rate at which  $L_i$  dissociates from the product  $EL_jL_2$ . In the latter two expressions, the indices  $i$  and  $j$  can equal one or two. We shall refer to this pathway two, or simply  $P_2$  as in (2b).

Though Zhuang et al. provided indirect evidence of the ligand switch in Zhuang et al. (2008), a direct demonstration of this process has not been possible with conventional techniques such as fluorescence microscopy, since such techniques introduce the possibility of modifying protein activity. Hence, scientists are using label-free optical biosensors to measure the rate constants in (2). By measuring the rate constants in (2), one could determine whether  $EL_2$  forms through direct binding or the catalysis-type ligand switching process. We note that the latter manifests itself mathematically with  ${}_2k_a = 0$ , while the former with  ${}^2_1k_a = {}^2_1k_d = {}_{1/2}k_a = {}_{1/2}k_d = 0$ .

However, the presence of multiple interacting components on the sensor surface complicates parameter estimation. In the present scenario, there are three species  $EL_1$ ,  $EL_1L_2$ , and  $EL_2$  at concentrations  $B_1(x, t)$ ,  $B_{12}(x, t)$ , and  $B_2(x, t)$ , and since optical biosensors typically measure only mass changes at the surface, lumped measurements of the form

$$\mathcal{S}(t) = s_1 \bar{B}_1(t) + (s_1 + s_2) \bar{B}_{12}(t) + s_2 \bar{B}_2(t) \tag{3}$$

are produced. In (3)

$$\bar{B}_i(t) = \frac{1}{x_{\max} - x_{\min}} \int_{x_{\min}}^{x_{\max}} B_i(x, t) dx \tag{4}$$

denotes the average reacting species concentration, for  $i = 1, 12, 2$ , and  $s_i$  denotes the molecular weight of  $L_i$ . The lumped signal (3) raises uniqueness concerns, since

more than one set of rate constants may possibly correspond to the same signal (3). Fortunately, through varying the uniform inflow concentrations of the ligands,  $C_1(0, y, t) = C_{1,u}$  and  $C_2(0, y, t) = C_{2,u}$ , one may resolve this ill-posedness in certain physically relevant scenarios (Edwards et al. 2017). This approach to identifying the correct set of rate constants in the presence of ambiguous data is related to the “global analysis” technique in biological literature (Karlsson and Fält 1997; Morton et al. 1995).

The presence of multiple interacting species and the lumped signal (3) complicate parameter estimation even for systems accurately described by the well-stirred kinetics approximation. However, in Edwards (1999), Edwards has shown that transport dynamics affect ligand binding in a thin boundary layer near the sensor surface. Hence, we begin in Sect. 2 by summarizing the relevant boundary layer equations, which take the form of a set of nonlinear integrodifferential equations (IDEs). In Sect. 3, it is shown that in experimentally relevant asymptotic limits our IDE model reduces to a much simpler set of ordinary differential equations (ODEs) which can be used for parameter estimation. To verify the accuracy of our ODE approximation, a numerical method is developed in Sect. 4.1. Convergence properties are examined in Sect. 4.2, and in Sect. 5 the accuracy of our ODE approximation is verified by comparing results of our ODE model with results from our numerical method described in Sect. 4. Conclusions and plans for future work are discussed in Sect. 6.

## 2 Governing Equations

For our purposes, biosensor experiments are partitioned into two phases: an injection phase and a wash phase. During the injection phase,  $L_1$  and  $L_2$  are injected into the biosensor via a buffer fluid at the uniform concentrations  $C_1(x, y, 0) = C_{1,u}$  and  $C_2(x, y, t) = C_{2,u}$ . Injection continues until the signal (3) reaches a steady state, at which point the biosensor is washed with the buffer fluid—this is the wash phase of the experiment. Only pure buffer is flowing through biosensor during the wash phase, not buffer containing ligand molecules. This causes all bound ligand molecules at the surface to dissociate and flow out of the biosensor, thereby preparing the device for another experiment. We first summarize the governing equations for the injection phase.

### 2.1 Injection Phase

To present our governing equations, we introduce the dimensionless variables:

$$\begin{aligned} \tilde{x} &= \frac{x}{L}, \quad \tilde{y} = \frac{y}{H}, \quad \tilde{t} = {}_1k_a C_{1,u} t, \quad \tilde{B}_i(x, t) = \frac{B_i(x, t)}{R_T}, \quad \tilde{C}_i(x, y, t) = \frac{C_i(x, y, t)}{C_{i,u}}, \\ {}_i\tilde{K}_a &= \frac{C_{i,u} \cdot {}_i^j k_a}{{}_1k_a \cdot {}_1k_a}, \quad {}_i\tilde{K}_d = \frac{k_d}{{}_1k_a \cdot {}_1k_a}, \quad \tilde{F}_r = \tilde{C}_r \tilde{D}_r, \quad \tilde{C}_r = \frac{C_{1,u}}{C_{2,u}}, \quad \tilde{D}_r = \frac{D_1}{D_2}. \end{aligned} \tag{5}$$

We have scaled the spatial variables with the instrument’s dimensions, time with the association rate of  $L_1$  onto an empty receptor, the bound ligand concentrations  $B_i$  with

the initial free receptor concentration, and the unbound ligand concentrations with their respective uniform inflow concentrations. The rate constants  $^j_i \tilde{K}_a$  and  $^j_i \tilde{K}_d$  are the dimensionless analogs of  $^j_i k_a$  and  $^j_i k_d$ . In the latter expressions the index  $i = 1, 2$ , whereas  $j = 1, 2$ , or can be blank. Furthermore,  $\tilde{F}_r$  measures the diffusion strength of each reacting species, as characterized by the product of the input concentrations and the diffusion coefficients. *Henceforth, we shall drop the tildes on our dimensionless variables for simplicity.* In particular, we denote the dimensionless sensogram reading as

$$S(t) = \frac{\mathcal{S}(t)}{R_T \cdot s_1} = \bar{B}_1(t) + \left(1 + \frac{s_2}{s_1}\right) \bar{B}_{12}(t) + \frac{s_2}{s_1} \bar{B}_2(t). \tag{6}$$

Moreover, we may use (4) to denote the *dimensionless* average concentration, as it is of the same form in both the dimensionless and dimensional contexts.

Applying the law of mass action to (2) gives the kinetics equations:

$$\begin{aligned} \frac{\partial B_1}{\partial t} &= (1 - B_\Sigma)C_1(x, 0, t) - {}_1K_d B_1 - \frac{1}{2}K_a B_1 C_2(x, 0, t) \\ &\quad + \frac{1}{2}K_d B_{12}, \end{aligned} \tag{7a}$$

$$\begin{aligned} \frac{\partial B_{12}}{\partial t} &= \frac{1}{2}K_a B_1 C_2(x, 0, t) - \frac{1}{2}K_d B_{12} + {}_1^2K_a B_2 C_1(x, 0, t) \\ &\quad - \frac{2}{1}K_d B_{12}, \end{aligned} \tag{7b}$$

$$\begin{aligned} \frac{\partial B_2}{\partial t} &= {}_2K_a (1 - B_\Sigma)C_2(x, 0, t) - {}_2K_d B_2 + \frac{2}{1}K_d B_{12} \\ &\quad - \frac{2}{1}K_a B_2 C_1(x, 0, t), \end{aligned} \tag{7c}$$

$$\mathbf{B}(x, 0) = \mathbf{0}, \tag{7d}$$

which hold on the reacting surface when  $y = 0$  and  $x \in [0, 1]$ . In (7d),  $\mathbf{B} = (B_1, B_{12}, B_2)^T$  is a vector in  $\mathbb{R}^3$  whose components contain the three bound state concentrations. In addition, the terms in Eqs. (7a)–(7c) are ordered in accordance with Figs. 2 and 3.

Edwards has shown (Edwards 1999) that transport effects dominate in a thin boundary layer near the reacting surface where diffusion and convection balance. Hence, the governing equations for  $C_i$  are

$$D_r \frac{\partial^2 C_1}{\partial \eta^2} = \eta \frac{\partial C_1}{\partial x}, \tag{8a}$$

$$\frac{\partial^2 C_2}{\partial \eta^2} = \eta \frac{\partial C_2}{\partial x}. \tag{8b}$$

In (8a)–(8b)  $\eta = \text{Pe}^{1/3}y$  is the boundary layer variable,  $\text{Pe} = VH^2/(LD_2) \gg 1$  is the Péclet number, and  $V$  is the characteristic velocity associated with our flow.

Since  $C_1$  is used up in the production of  $B_1$  and  $B_{12}$ , and  $C_2$  is used up in the production of  $B_{12}$  and  $B_2$ , we have the diffusive flux conditions:

$$\frac{\partial C_1}{\partial \eta}(x, 0, t) = \frac{Da}{F_r} \left( \frac{\partial B_1}{\partial t} + \frac{\partial B_{12}}{\partial t} \right), \tag{8c}$$

$$\frac{\partial C_2}{\partial \eta}(x, 0, t) = Da \left( \frac{\partial B_{12}}{\partial t} + \frac{\partial B_2}{\partial t} \right). \tag{8d}$$

Equations (8a)–(8d) reflect the fact that in the boundary layer  $C$  is in a quasi-steady state where change is driven solely by the surface reactions (8c)–(8d). Then, given the inflow and matching conditions

$$C_i(0, \eta, t) = 1, \tag{8e}$$

$$\lim_{\eta \rightarrow \infty} C_i(x, \eta, t) = 1, \tag{8f}$$

the solution to (8) is given by

$$C_1(x, 0, t) = 1 - \frac{D_r^{1/3} Da}{F_r \Gamma(2/3) 3^{1/3}} \int_0^x \left( \frac{\partial B_1}{\partial t} + \frac{\partial B_{12}}{\partial t} \right) (x - \nu, t) \frac{d\nu}{\nu^{2/3}}, \tag{9a}$$

$$C_2(x, 0, t) = 1 - \frac{Da}{\Gamma(2/3) 3^{1/3}} \int_0^x \left( \frac{\partial B_{12}}{\partial t} + \frac{\partial B_2}{\partial t} \right) (x - \nu, t) \frac{d\nu}{\nu^{2/3}}. \tag{9b}$$

See Edwards (1999) for details of a similar calculation. During the injection phase, the bound state concentration is then governed by (7) using (9).

In (8c)–(8d) and (9)

$$Da = \frac{1 k_a R_T (HL)^{1/3}}{(VD^2)^{1/3}} \tag{10}$$

is the Damköhler number—a key dimensionless parameter which measures the speed of reaction relative to the transport into the surface. In the experimentally relevant parameter regime of  $Da \ll 1$ , the timescale for transport into the surface is much faster than the timescale for reaction. In this case there is only a weak coupling between the two processes, and (9) shows that the unbound concentration at the surface is only a perturbation away from uniform inlet concentration. When  $Da \rightarrow 0$  in (7) using (9), one recovers the well-stirred approximation in which transport into the surface completely decouples from reaction.

On the other hand, when  $Da = O(1)$  the two processes occur on the same timescale, and *ligand depletion effects* become more evident. This is a phenomenon in which ligand molecules are transported into the surface to bind with receptor sites upstream, before they bind with receptor sites downstream. Mathematically, this is reflected in the convolution integrals in (9). When  $x \ll 1$ , the convolution integral influences the unbound concentration at the surface less than when  $x$  is larger.

A sample space–time curve for each of the reacting species concentrations  $B_i(x, t)$  is depicted in Fig. 4, where we have shown the results of our numerical simulations

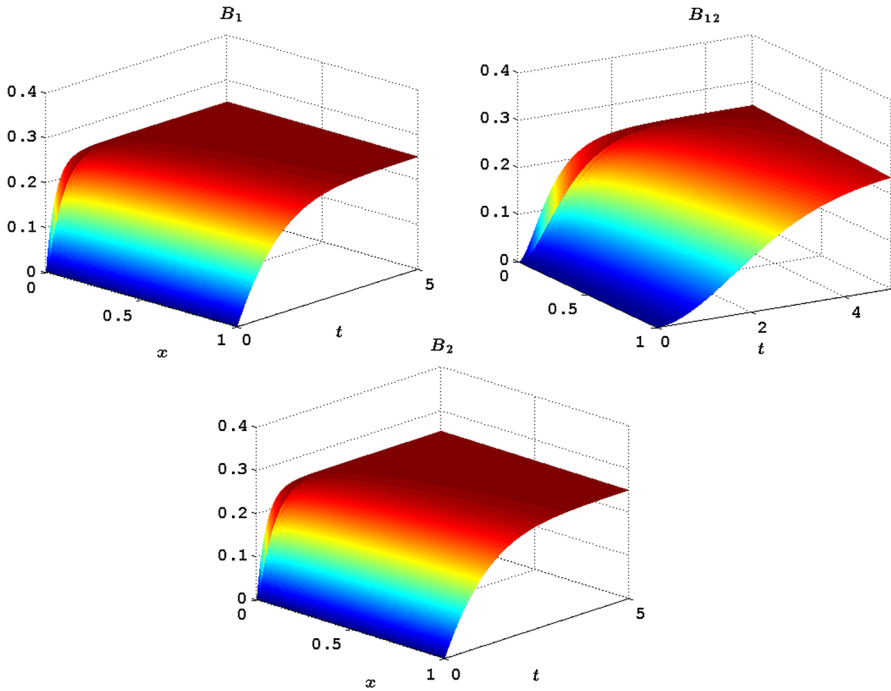


**Fig. 4** (Color figure online) Injection phase of biosensor experiment, up to  $t = 5$ , obtained through solving (7), (9) with the numerical method described in Sect. 4. All rate constants were taken equal to one, and  $Da$  is taken equal to two to visualize upstream ligand depletion, which is especially evident in  $B_{12}$

described in Sect. 4. The  $x$ -axis represents the sensor, and  $t$ -axis represents time. Injection begins at  $t = 0$ , and ligand molecules bind with receptor sites as they are transported into the surface. Binding proceeds as the injection continues; finally, each of the concentrations achieves a chemical equilibrium in which there is a balance between association and dissociation. Observe the spatial heterogeneity present in each of the bound state concentrations—the reaction proceeds faster near the inlet at  $x = 0$  than the rest of the surface. This is precisely the ligand depletion phenomenon described in the above paragraph and is particularly evident in the surface plot of  $B_{12}$ . This is because in this simulation we have taken all of the rate constants equal to one, and either  $EL_1$  or  $EL_2$  must be present in order for  $EL_1L_2$  to form. Thus, in this case  $EL_1L_2$  experiences effectively twice the ligand depletion of the other reacting species.

Furthermore, one may notice an apparent discontinuity in each of the surface plots depicted in Fig. 4—this reflects the weakly singular nature of the functions which we are attempting to approximate. When  $x \ll 1$ , one may show  $\mathbf{B}$  has the perturbation expansion

$$\mathbf{B}(x, t) = {}^0\mathbf{B}(t) + Da x^{1/3} \cdot {}^1\mathbf{B}(t) + O(Da^2 x^{2/3}) \tag{11}$$

(this is simply (19) for  $x \ll 1$ ). It therefore follows that

$$\frac{\partial \mathbf{B}}{\partial x}(x, t) = \frac{\text{Da} \mathbf{1B}(t)}{3x^{2/3}} + O\left(\frac{\text{Da}^2}{x^{1/3}}\right). \tag{12}$$

Hence, although the function  $\mathbf{B}$  is well defined and continuous near  $x = 0$ , it has a vertical tangent at  $x = 0$ . The weakly singular nature of  $\mathbf{B}$  is magnified since  $\text{Da} = 2$ . To resolve this region, one may think to adaptively change  $\Delta x$  with the magnitude of  $\partial \mathbf{B} / \partial x$ . However, because the sensogram reading  $S(t)$  is computed over the region  $[x_{\min}, x_{\max}]$ , we are not concerned with resolving this region and a uniform step size is sufficient. Moreover, our convergence results in Sect. 4.2 demonstrate that a lack of resolution at  $x = 0$  does not affect our results in the region of interest  $[x_{\min}, x_{\max}]$ .

### 2.2 Wash Phase

We now summarize the relevant equations for the wash phase. In practice the injection phase is run until the bound state concentration reaches a steady state (Rich and Myszka 2009). This implies that because the bound ligand concentration evolves on a much slower timescale than the unbound ligand concentration (Edwards 1999), the unbound ligand concentration will have also reached steady state by the time the wash phase begins. In particular, the unbound concentration on the surface will be uniform by the time the wash phase starts—i.e.,  $C_i(x, 0, 0) = 1$ . Thus, the kinetics equations are given by (7), with (35d) replaced by the steady solution to (7) during the injection phase:

$$\mathbf{B}(x, 0) = A^{-1} \mathbf{f}, \tag{13a}$$

$$A = \begin{pmatrix} (1 + {}_1K_d + \frac{1}{2}K_a) & 1 - \frac{1}{2}K_d & 1 \\ -\frac{1}{2}K_a & (\frac{1}{2}K_d + \frac{2}{1}K_d) & -\frac{2}{1}K_a \\ {}_2K_a & {}_2K_a - \frac{2}{1}K_d & ({}_2K_a + {}_2K_d + \frac{2}{1}K_a) \end{pmatrix}, \tag{13b}$$

$$\mathbf{f} = \begin{pmatrix} 1 \\ 0 \\ {}_2K_a \end{pmatrix}. \tag{13c}$$

Equations similar to (8) hold:

$$C_i(0, \eta, t) = 0, \tag{14a}$$

$$\lim_{\eta \rightarrow \infty} C_i(x, \eta, t) = 0. \tag{14b}$$

Equation (14a) is the inflow condition, and (14b) expresses the requirement that the concentration in the boundary layer must match the concentration  $C_i(x, y, t) = 0$  in the outer region. Moreover, as in the injection phase one can use (8a)–(8d) together with (14) to show:

$$C_1(x, 0, t) = -\frac{D_r^{1/3} Da}{F_r \Gamma(2/3) 3^{1/3}} \int_0^x \left( \frac{\partial B_1}{\partial t} + \frac{\partial B_{12}}{\partial t} \right) (x - v, t) \frac{dv}{x^{2/3}}, \tag{15a}$$

$$C_2(x, 0, t) = -\frac{Da}{\Gamma(2/3) 3^{1/3}} \int_0^x \left( \frac{\partial B_{12}}{\partial t} + \frac{\partial B_2}{\partial t} \right) (x - v, t) \frac{dv}{v^{2/3}}. \tag{15b}$$

Thus, during the wash phase the bound state evolution is governed by (7a)–(7c), (13), and (15).

### 3 Effective Rate Constant Approximation

During both phases of the experiment, the bound state concentration  $\mathbf{B}(x, t)$  obeys a nonlinear set of IDEs which is hopeless to solve in closed form. However, we are ultimately interested in the average concentration  $\overline{\mathbf{B}}(t)$ , rather than the spatially dependent function  $\mathbf{B}(x, t)$ , since from  $\overline{\mathbf{B}}(t)$  we can construct the sensogram signal (6) (the quantity of interest). Thus, we seek to find an approximation to  $\overline{\mathbf{B}}(t)$ , and begin by finding one during the injection phase. We first average each side of (7), with  $C_1(x, 0, t)$  and  $C_2(x, 0, t)$  given by (9), in the sense of (4). Immediately, we are confronted with terms such as

$$\overline{B_1 C_2} = B_1 \overline{\left( 1 - \frac{Da}{3^{1/3} \Gamma(2/3)} \int_0^x \left( \frac{\partial B_{12}}{\partial t} + \frac{\partial B_2}{\partial t} \right) \frac{dv}{(x - v)^{2/3}} \right)}, \tag{16}$$

on the right-hand side of (7a). In the experimentally relevant case of small Da, we are motivated to expand  $\mathbf{B}(x, t)$  in a perturbation series:

$$\mathbf{B}(x, t) = {}^0\mathbf{B}(x, t) + O(Da). \tag{17}$$

In this limit, the leading order of (9) is just  $C_i = 1$ . Using this result in (7), we have that the governing equation for  ${}^0\mathbf{B}$  is independent of  $x$ :

$$\frac{d {}^0\mathbf{B}}{dt} = -A {}^0\mathbf{B} + \mathbf{f},$$

where  $A$  is given by (13b) and  $\mathbf{f}$  by (13c). Hence, the leading-order approximation

$${}^0\mathbf{B}(t) = A^{-1} (I - e^{-At}) \mathbf{f} \tag{18}$$

is independent of space. Substituting (18) into (9), the time-dependent terms may be factored out of the integrand, leaving the spatial dependence of  $C_j$  varying as  $x^{1/3}$ . This is the only spatial variation in (7) at  $O(Da)$ ; hence, we may write

$$\mathbf{B}(x, t) = {}^0\mathbf{B}(t) + Da x^{1/3} \cdot {}^1\mathbf{B}(t) + O(Da^2). \tag{19}$$

As a result of (19), we have the relation

$$Da B_i(x, t) = Da {}^0B_i(t) + O(Da^2), \tag{20}$$

which may be used to show the right-hand side of (16) is equal to

$$\begin{aligned} \bar{B}_1 - \text{Da} \bar{h} \cdot {}^0B_1 \left( \frac{d {}^0B_{12}}{dt} + \frac{d {}^0B_2}{dt} \right) + O(\text{Da}^2), \\ h(x) = \frac{3^{2/3} x^{1/3}}{\Gamma(2/3)}. \end{aligned} \tag{21}$$

We then average (20) and use the resulting relation in (21) to show the right-hand side of (16) reduces to:

$$\overline{B_1 C_2} = \bar{B}_1 \left[ 1 - \text{Da} \bar{h} \left( \frac{d \bar{B}_{12}}{dt} + \frac{d \bar{B}_2}{dt} \right) \right] + O(\text{Da}^2).$$

In this manner, we can derive a set of nonlinear ODEs for  $\bar{\mathbf{B}}(t)$  of the form:

$$\frac{d \bar{\mathbf{B}}}{dt} = M^{-1}(\bar{\mathbf{B}})(-A \bar{\mathbf{B}} + \mathbf{f}) + O(\text{Da}^2), \tag{22a}$$

$$\bar{\mathbf{B}}(0) = \mathbf{0}, \tag{22b}$$

where

$$M(\bar{\mathbf{B}}) = I + \text{Da} N(\bar{\mathbf{B}}), \tag{22c}$$

$$N(\bar{\mathbf{B}}) = \begin{pmatrix} \frac{D_r^{1/3} \bar{h}}{F_r} (1 - \bar{B}_\Sigma) & \frac{D_r^{1/3} \bar{h}}{F_r} (1 - \bar{B}_\Sigma) - \frac{1}{2} K_a \bar{h} \cdot \bar{B}_1 & -\frac{1}{2} K_a \bar{h} \cdot \bar{B}_1 \\ \frac{1}{2} K_a \bar{h} \cdot \bar{B}_1 & \frac{1}{2} K_a \bar{h} \cdot \bar{B}_1 + \frac{2}{1} K_a \left( \frac{D_r^{1/3} \bar{h}}{F_r} \right) \bar{B}_2 & \frac{2}{1} K_a \left( \frac{D_r^{1/3} \bar{h}}{F_r} \right) \bar{B}_2 \\ -\frac{1}{2} K_a \left( \frac{D_r^{1/3} \bar{h}}{F_r} \right) \bar{B}_2 & -\frac{1}{2} K_a \left( \frac{D_r^{1/3} \bar{h}}{F_r} \right) \bar{B}_2 + \frac{2}{2} K_a \bar{h} (1 - \bar{B}_\Sigma) & \frac{2}{2} K_a \bar{h} (1 - \bar{B}_\Sigma) \end{pmatrix}. \tag{22d}$$

We have also derived a set of ERC equations for the wash phase, and they take the form:

$$\frac{d \bar{\mathbf{B}}}{dt} = M^{-1}(\bar{\mathbf{B}})(-\mathcal{D} \bar{\mathbf{B}}) + O(\text{Da}^2), \tag{23a}$$

$$\bar{\mathbf{B}}(0) = A^{-1} \mathbf{f}, \tag{23b}$$

$$\mathcal{D} = \begin{pmatrix} {}_1K_d & -\frac{1}{2} K_d & 0 \\ 0 & \frac{2}{1} K_d + \frac{1}{2} K_d & 0 \\ 0 & -\frac{2}{1} K_d & {}_2K_d \end{pmatrix}, \tag{23c}$$

where  $M(\bar{\mathbf{B}})$  is as in (22c)

Following [Edwards and Jackson \(2002\)](#), we refer to the ordinary differential equation (ODE) systems (22) and (23) as our *effective rate constant (ERC) equations*. A

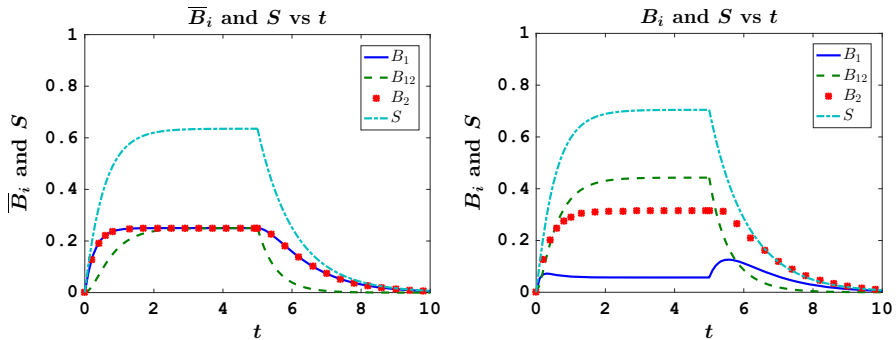


**Fig. 5** (Color figure online) *Left* the solution of injection phase ERC equations (22) is depicted from  $t = 0$  to  $t = 5$ , and the solution of the wash phase ERC equations (23) is depicted from  $t = 5$  to  $t = 10$ . Here all of the rate constants were taken equal to 1. *Right* the injection phase (22) is depicted from  $t = 0$  to  $t = 5$ , and the wash phase (23) is depicted from  $t = 5$  to  $t = 10$ . Here all of the rate constants were taken equal to 1 except  $\frac{1}{2}K_a = 10$ . Both the Damköhler number was taken equal to  $Da = 0.1$

significant advantage of our ERC equations is that these ODEs are far easier to solve numerically than their IDE counterparts. To solve (22) or (23), one may simply apply their linear multistage or multistep formula of choice. This feature renders our ERC equations attractive for data analysis, since they can be readily implemented into a regression algorithm when attempting to determine the rate constants associated with the reactions (2). Since experimental data are still forthcoming, we do not employ a regression algorithm to fit the rate constants in (22) and (23) to biosensor data. Synthetic data for the kinetic rate constants were used in our numerical simulations.

Solutions of our ERC equations for different parameter values are depicted in Fig. 5. First, consider the solutions depicted on the left. Here the injection phase (22) has been run from  $t = 0$  to  $t = 5$ , and the wash phase (23) has been run from  $t = 5$  to  $t = 10$ . Furthermore, all rate constants were taken equal to one and the Damköhler number was  $Da = 0.1$ . During the injection phase, it is seen that  $\bar{B}_1$  and  $\bar{B}_2$  reach equilibrium after approximately 1 s, while  $\bar{B}_{12}$  takes approximately 2 s. This is not a surprise: We are injecting equal amounts of both ligands, all the rate constants are the same, and either  $EL_1$  or  $EL_2$  must already be present in order for  $EL_1L_2$  to form. The equality of the rate constants is also the reason why all three species attain the same steady state. Mathematically, the steady state of  $\mathbf{B}$  during the injection phase is given by (13a), and one can readily verify that  $A^{-1}\mathbf{f} = (1/4, 1/4, 1/4)^T$  when all of the rate constants are equal to one. Physically, each of the species ultimately achieves the same balance between association and dissociation. Furthermore, the fact that all of the rate constants are the same is the reason why  $\bar{B}_{12}$  decays to zero faster than the other two species:  $EL_1L_2$  transitions to either  $EL_1$  or  $EL_2$  at the same rate as the latter two species transition into an empty receptor  $E$ .

Now consider the solutions depicted on the right in Fig. 5. As with the previous case, the injection phase has been run from  $t = 0$  to  $t = 5$  and the wash phase has been run from  $t = 5$  to  $t = 10$ . However, this time, all the rate constants have been taken equal to one except  $\frac{1}{2}K_a$ , which was taken equal to  $\frac{1}{2}K_a = 10$ . During the injection phase, it is seen that  $\bar{B}_1$  quickly reaches a local maximum and then decreases

to steady state. Since  $\frac{1}{2}K_a$  is an order of magnitude larger than the other rate constants, after a short period of time  $L_2$ , molecules bind with  $EL_1$  at a faster rate than  $L_1$  molecules bind with empty receptor sites. This results in the chemical equilibrium between  $EL_1$  and  $EL_1L_2$  depicted on the right in Fig. 5. From these observations, it is clear why the steady-state value of  $\bar{B}_{12}$  is larger than the previous case. However, it may be counterintuitive to observe that  $\bar{B}_2$  reaches a larger steady-state value in the solutions depicted on the right than the solutions depicted to the left. Although one may think the vast majority  $L_2$  molecules should be used in forming  $EL_1L_2$ , the increase in  $EL_1L_2$  also increases the concentration of empty receptor sites. The continuous injection of  $L_2$  therefore drives the average concentration  $\bar{B}_2$  to a larger steady-state value. During the wash phase, it is seen that  $\bar{B}_1$  reaches a global maximum after approximately  $t \approx 5.75$  s. The increase in  $\bar{B}_1$  during the wash phase is a direct consequence of  $L_2$  molecules dissociating from  $EL_1L_2$ . Since only pure buffer is flowing through the biosensor during the wash phase, it is shown in Fig. 5 that each of the average concentrations  $\bar{B}_i$  decay to zero.

### 4 Numerics

To verify the  $O(Da^2)$  accuracy of our ERC approximation derived in Sect. 3, we now develop a numerical approximation to the IDE system (7), where  $C_1(x, 0, t)$  and  $C_2(x, 0, t)$  are given by (9). We focus on the injection phase, since the wash phase is similar. Our approach is based on the numerical method described in [Edwards and Jackson \(2002\)](#). Semi-implicit methods have been previously used with great success to solve reaction–diffusion equations ([Nie et al. 2006](#)), as they are typically robust, efficient, and accurate. Similarly, in our problem we exploit the structure of the integrodifferential operator, which naturally suggests a semi-implicit method in time. Moreover, since our method is semi-implicit in time, we avoid the expense and complication of solving a nonlinear system at each time step. Convergence properties and remarks concerning stability are discussed in Sect. 4.2; however, we first turn our attention to deriving our numerical method in Sect. 4.1.

#### 4.1 Semi-implicit Finite Difference Algorithm

We discretize the spatial interval  $[0, 1]$  by choosing  $N + 1$  equally spaced discretization nodes  $x_i = i \Delta x$ , for  $i = 0, \dots, N$ , and discretize time by setting  $t_n = n \Delta t$ , for  $n = 0, \dots$ . Having chosen our discretization nodes and time steps, we seek to discretize (7), where  $C_1(x, 0, t)$  and  $C_2(x, 0, t)$  are given by (9). Note that this requires discretizing both the time derivatives and the convolution integrals; we first turn our attention to the latter and focus on  $C_1(x, 0, t)$ . We would like to apply the trapezoidal rule to spatially discretize (9a); however, the integrand of  $C_1(x, 0, t)$  is singular when  $v = 0$ . To handle the singularity, we subtract and add

$$\left( \frac{\partial B_1}{\partial t} + \frac{\partial B_{12}}{\partial t} \right) (x - v, t)|_{v=0} \tag{24}$$

from the integrand. Doing so yields

$$C_1(x, 0, t) = 1 - \frac{D_r^{1/3} Da}{F_r 3^{1/3} \Gamma(2/3)} \left\{ \int_0^x \left[ \left( \frac{\partial B_1}{\partial t} + \frac{\partial B_{12}}{\partial t} \right) (x - v, t) - \left( \frac{\partial B_1}{\partial t} + \frac{\partial B_{12}}{\partial t} \right) (x, t) \right] \frac{dv}{v^{2/3}} + 3x^{1/3} \left( \frac{\partial B_1}{\partial t} + \frac{\partial B_{12}}{\partial t} \right) (x, t) \right\}, \tag{25}$$

where we have used the fact that (24) is independent of  $v$ . Then choosing a discretization node  $x = x_i$  and a time step  $t = t_n$ , we apply the trapezoidal rule to (25) to obtain

$$C_1(x_i, 0, t_n) = 1 - \frac{D_r^{1/3} Da}{F_r 3^{1/3} \Gamma(2/3)} \left\{ 0 \cdot \frac{\Delta x}{2} + \sum_{j=1}^{i-1} \left[ \left( \frac{\partial B_1}{\partial t} + \frac{\partial B_{12}}{\partial t} \right) (x_i - x_j, t_n) - \left( \frac{\partial B_1}{\partial t} + \frac{\partial B_{12}}{\partial t} \right) (x_i, t_n) \right] \frac{\Delta x}{x_j^{2/3}} + \left[ \left( \frac{\partial B_1}{\partial t} + \frac{\partial B_{12}}{\partial t} \right) (0, t_n) - \left( \frac{\partial B_1}{\partial t} + \frac{\partial B_{12}}{\partial t} \right) (x_i, t_n) \right] \frac{\Delta x}{2x_i^{2/3}} + 3x_i^{1/3} \left( \frac{\partial B_1}{\partial t} + \frac{\partial B_{12}}{\partial t} \right) (x_i, t_n) \right\}, \tag{26}$$

when  $x_i > 0$ ; simply evaluating (25) at  $x = x_0$  gives  $C(x_0, 0, t_n) = 1$ . The first term in the sum is zero, because in a similar manner to Appendix B of Zumbum (2013) we have

$$\begin{aligned} & \lim_{v \rightarrow 0} \left( \frac{\partial B_k}{\partial t} (x - v, t_n) - \frac{\partial B_k}{\partial t} (x, t) \right) \frac{1}{v^{2/3}} \\ &= \lim_{v \rightarrow 0} v^{1/3} \left( \frac{\partial B_k}{\partial t} (x - v, t_n) - \frac{\partial B_k}{\partial t} (x, t) \right) \frac{1}{v}, \end{aligned} \tag{27}$$

which implies

$$\lim_{v \rightarrow 0} \left( \frac{\partial B_k}{\partial t} (x - v, t_n) - \frac{\partial B_k}{\partial t} (x, t) \right) \frac{1}{v^{2/3}} = \lim_{v \rightarrow 0} v^{1/3} \frac{\partial^2 B_k}{\partial x \partial t} (x, t) = 0, \tag{28}$$

for  $k = 1, 12$ , or  $2$ . The last equality follows since we expect  $\partial B_i / \partial t$  to be sufficiently regular for fixed  $x > 0$ . The expansion (19) shows that this is certainly true when  $Da \ll 1$ ; however, when  $Da = O(1)$  or larger, the nonlinearity in (7) renders any analytic approximation to  $B_i$  beyond reach. Our results in Sect. 4.2 show that our method indeed converges when  $Da = O(1)$  or larger.

We now turn our attention to discretizing the time derivatives. We denote our approximation to  $B_j(x_i, t_n)$  by

$$B_j(x_i, t_n) \approx B_{i,n}^j, \tag{29}$$

and approximate the time derivatives through the formula

$$\frac{\partial B_j}{\partial t}(x_i, t_n) \approx \frac{B_{i,n}^j - B_{i,n-1}^j}{\Delta t} := \frac{\Delta B_{i,n}^j}{\Delta t}. \tag{30}$$

Our approximation (30) holds for all reacting species  $j = 1, 12, 2$ , each of our discretization nodes  $x_i$ , and each time step  $t_n$ . As we shall show below, we treat  $\Delta B_{i,n}^j$  as separate variable used to update  $B_{i,n}^j$  at each iteration of our algorithm.

With our time derivatives discretized as (30), the fully discretized version of  $C_1(x, 0, t)$  is given by substituting (30) into (26):

$$\begin{aligned} C_{i,n}^1 = & 1 - \frac{D_r^{1/3} Da}{F_r 3^{1/3} \Gamma(2/3)} \left\{ \sum_{j=1}^{i-1} \left[ \left( \frac{\Delta B_{i-j,n}^1}{\Delta t} + \frac{\Delta B_{i-j,n}^{12}}{\Delta t} \right) \right. \right. \\ & \left. \left. - \left( \frac{\Delta B_{i,n}^1}{\Delta t} + \frac{\Delta B_{i,n}^{12}}{\Delta t} \right) \right] \frac{\Delta x}{x_j^{2/3}} \right. \\ & \left. + \left[ \left( \frac{\Delta B_{0,n}^1}{\Delta t} + \frac{\Delta B_{0,n}^{12}}{\Delta t} \right) - \left( \frac{\Delta B_{i,n}^1}{\Delta t} + \frac{\Delta B_{i,n}^{12}}{\Delta t} \right) \right] \right. \\ & \left. \frac{\Delta x}{2x_i^{2/3}} + 3x_i^{1/3} \left( \frac{\Delta B_{i,n}^1}{\Delta t} + \frac{\Delta B_{i,n}^{12}}{\Delta t} \right) \right\}, \tag{31a} \end{aligned}$$

for  $i > 0$ , and  $C_{0,n}^1 = 1$ . The function  $C_2(x, 0, t)$  has a similar discretization which we denote as  $C_2(x_i, 0, t_n) \approx C_{i,n}^2$ . Thus, our numerical method takes the form:

$$\begin{aligned} \frac{\Delta B_{i,n+1}^1}{\Delta t} = & (1 - B_{i,n}^\Sigma) C_{i,n+1}^1 - {}_1K_d B_{i,n}^1 \\ & - \frac{1}{2} K_a B_{i,n}^1 C_{i,n+1}^2 + \frac{1}{2} K_d B_{i,n}^{12}, \tag{31b} \end{aligned}$$

$$\begin{aligned} \frac{\Delta B_{i,n+1}^{12}}{\Delta t} = & \frac{1}{2} K_a B_{i,n}^1 C_{i,n+1}^2 - \frac{1}{2} K_d B_{i,n}^{12} \\ & + \frac{2}{1} K_a B_{i,n}^2 C_{i,n+1}^1 - \frac{2}{1} K_d B_{i,n}^{12}, \tag{31c} \end{aligned}$$

$$\begin{aligned} \frac{\Delta B_{i,n+1}^2}{\Delta t} = & {}_2K_a (1 - B_{i,n}^\Sigma) C_{i,n+1}^2 - {}_2K_d B_{i,n}^2 \\ & + \frac{2}{1} K_d B_{i,n}^{12} - \frac{2}{1} K_a B_{i,n}^2 C_{i,n+1}^1. \tag{31d} \end{aligned}$$

We enforce the initial condition (35d) at our  $N + 1$  discretization nodes through the condition  $B_{i,0}^j = 0$  for  $j = 1, 12, 2$ , and  $i = 1, \dots, N$ . Observe that our method (31) is semi-implicit rather than fully implicit. This renders (31) linear in  $\Delta B_{i,n+1}^j$ , and as a result we can write

$$\frac{\Delta \mathbf{B}_{i,n+1}}{\Delta t} = M_{i,n}^{-1}(\mathbf{B}_{i,n}) (A_{i,n+1}^{-1} \mathbf{B}_{i,n} + \mathbf{f}_{i,n+1}), \tag{32a}$$

where  $\mathbf{B}_{i,n} = (B_{i,n}^1, B_{i,n}^{12}, B_{i,n}^2)^T$ . Hence, by using a method which is only semi-implicit in time we avoid the expense and complication of solving a nonlinear system at each time step. Having solved for  $\Delta\mathbf{B}_{i,n+1}$  using (32a), we march forward in time at a given node  $x_i$  through the formula

$$\mathbf{B}_{i,n+1} = \mathbf{B}_{i,n} + \frac{1}{2}(3\Delta\mathbf{B}_{i,n+1} - \Delta\mathbf{B}_{i,n}), \tag{32b}$$

which is analogous to a second-order Adams–Bashforth formula.

In addition, we chose a method that is implicit in  $C_1(x, 0, t)$  and  $C_2(x, 0, t)$  also due to the form of the convolution integrals. From (9) we see  $C_1(x, 0, t)$  and  $C_2(x, 0, t)$  depend on  $B_j(v, t)$  only for  $v \leq x$ . Thus, by choosing a method that is implicit in  $C_1(x, 0, t)$  and  $C_2(x, 0, t)$ , we are able to use the *updated values* of  $B_j(x, t)$  in the convolution integrals by first computing the solution at  $x = 0$  and marching our way downstream at each time step.

To make this notion more precise, we note that in (32a) the matrix  $M_{i,n}^{-1}(\mathbf{B}_{i,n})$  depends only upon  $\mathbf{B}_{i,n}$ ; however, because of the convolution integrals  $C_{i,n+1}^1$  and  $C_{i,n+1}^2$ , the matrix  $A_{i,n+1}$  and vector  $\mathbf{f}_{i,n+1}$  depend upon  $\mathbf{B}_{l,n+1}$  for  $l < i$ . Thus, at each time step  $n + 1$  we first determine  $\mathbf{B}_{0,n+1}$ . Next, we increment  $i$  and use the value of  $\mathbf{B}_{0,n+1}$  in (32) to determine  $\mathbf{B}_{1,n+1}$ . We proceed by iteratively marching our way downstream from  $x_2$  to  $x_N$  to determine  $\mathbf{B}_{2,n+1}, \dots, \mathbf{B}_{N,n+1}$ . Intuitively, the updated information from the convolution integral flows downstream from left to right at each time step. We may repeat this procedure for as many time steps as we wish. In addition, we remark that the formula (31) was initialized with one step of Euler’s method.

Furthermore, with our finite difference approximation to  $\mathbf{B}(x, t)$ , we can determine the average quantity

$$\bar{\mathbf{B}}(t) = (\bar{B}_1(t), \bar{B}_{12}(t), \bar{B}_2(t))^T \tag{33}$$

with the trapezoidal rule

$$\bar{\mathbf{B}}(t_n) \approx \frac{1}{x_{\max} - x_{\min}} \left( \frac{\Delta x}{2} \mathbf{B}_{m,n} + \Delta x \sum_{i=m+1}^{M-1} \mathbf{B}_{i,n} + \frac{\Delta x}{2} \mathbf{B}_{M,n} \right). \tag{34}$$

In (34), the indices  $i = m$  and  $i = M$  correspond to  $x_{\min} = m\Delta x$  and  $x_{\max} = M\Delta x$ . Our nodes were chosen to align with  $x_{\min}$  and  $x_{\max}$  to avoid interpolation error.

## 4.2 Convergence Study

### 4.2.1 Spatial Convergence

We now examine the spatial rate of convergence of our numerical method. Since from  $\bar{\mathbf{B}}$  we can compute the quantity of interest (6), we derive estimates for the rate at which our numerical approximation converges to  $\bar{\mathbf{B}}$ . Furthermore, because systems (7), (9)

are nonlinear, our analysis will focus on the experimentally relevant case of  $Da \ll 1$ . In addition, we will derive estimates only for the injection phase of the experiment, since the wash phase is similar.

To proceed, we consider the average variant of (7), (9). Averaging (7) in the sense of (4) gives:

$$\frac{d\bar{B}_1}{dt} = \overline{(1 - B_\Sigma)C_1(x, 0, t)} - {}_1K_d\bar{B}_1 - \frac{1}{2}K_a\overline{B_1C_2(x, 0, t)} + \frac{1}{2}K_d\bar{B}_{12}, \tag{35a}$$

$$\frac{d\bar{B}_{12}}{dt} = \frac{1}{2}K_a\overline{B_1C_2(x, 0, t)} - \frac{1}{2}K_d\bar{B}_{12} + \frac{1}{2}K_a\overline{B_2C_1(x, 0, t)} - \frac{1}{2}K_d\bar{B}_{12}, \tag{35b}$$

$$\frac{d\bar{B}_2}{dt} = {}_2K_a\overline{(1 - B_\Sigma)C_2(x, 0, t)} - {}_2K_d\bar{B}_2 + \frac{1}{2}K_d\bar{B}_{12} - \frac{1}{2}K_a\overline{B_2C_1(x, 0, t)}. \tag{35c}$$

$$\bar{\mathbf{B}}(0) = \mathbf{0}. \tag{35d}$$

As in Sect. 4.1, we handle the singularity in (9a) by adding and subtracting (24) from the integrand of (9a) to write  $C_1(x, 0, t)$  as in (25). The unbound ligand concentration  $C_2(x, 0, t)$  has a representation analogous to (25). In the following analysis, we limit our attention to (35a), since the analysis for Eqs. (35b)–(35c) is nearly identical.

We proceed by analyzing each of the terms in (35a):

$$- {}_1K_d\bar{B}_1, \tag{36a}$$

$$\frac{1}{2}K_d\bar{B}_{12}, \tag{36b}$$

$$\overline{C_1(x, 0, t)}, \tag{36c}$$

$$- \overline{B_\Sigma C_1(x, 0, t)}, \tag{36d}$$

$$- \frac{1}{2}K_a\overline{B_1C_2(x, 0, t)}. \tag{36e}$$

Upon inspecting (25) and using linearity of the averaging operator, we see that three terms contribute to (36c):

$$\bar{1} \tag{37a}$$

$$- \frac{D_r^{1/3}Da}{F_r 3^{1/3}\Gamma(2/3)} \int_0^x \left( \frac{\partial B_1}{\partial t} + \frac{\partial B_{12}}{\partial t} \right) (x - \nu, t) - \left( \frac{\partial B_1}{\partial t} + \frac{\partial B_{12}}{\partial t} \right) (x, t) \frac{d\nu}{\nu^{2/3}}, \tag{37b}$$

$$3x^{1/3} \left( \frac{\partial B_1}{\partial t} + \frac{\partial B_{12}}{\partial t} \right). \tag{37c}$$

In a similar manner, (36d) and (36e) each imply that we incur error from the terms:

$$-\overline{B_\Sigma} \tag{38a}$$

$$\frac{D_r^{1/3} Da B_\Sigma}{F_r 3^{1/3} \Gamma(2/3)} \int_0^x \left( \frac{\partial B_1}{\partial t} + \frac{\partial B_{12}}{\partial t} \right) (x - \nu, t) - \left( \frac{\partial B_1}{\partial t} + \frac{\partial B_{12}}{\partial t} \right) (x, t) \frac{d\nu}{\nu^{2/3}}, \tag{38b}$$

$$-3x^{1/3} B_\Sigma \left( \frac{\partial B_1}{\partial t} + \frac{\partial B_{12}}{\partial t} \right), \tag{38c}$$

$$-\frac{1}{2} K_a B_1 \tag{38d}$$

$$\frac{\frac{1}{2} K_a Da B_1}{3^{1/3} \Gamma(2/3)} \int_0^x \left( \frac{\partial B_{12}}{\partial t} + \frac{\partial B_2}{\partial t} \right) (x - \nu, t) - \left( \frac{\partial B_{12}}{\partial t} + \frac{\partial B_2}{\partial t} \right) (x, t) \frac{d\nu}{\nu^{2/3}}, \tag{38e}$$

$$-3\frac{1}{2} K_a x^{1/3} B_1 \left( \frac{\partial B_{12}}{\partial t} + \frac{\partial B_2}{\partial t} \right). \tag{38f}$$

Let us denote the trapezoidal rule of a function  $f(x)$  over the interval  $[a, b]$  by  $\mathcal{T}(f(x), [a, b])$ . Then since  $\mathcal{T}(1, [x_{\min}, x_{\max}])$  is exact, the term (37a) does not contribute to the spatial discretization error.

Next, we decompose the expansion (19) into its individual components to obtain

$$B_j(x, t) = {}^0 B_j(t) + Da x^{1/3} \cdot {}^1 B_j(t) + O(x^{2/3} Da^2), \tag{39}$$

for  $j = 1, 12, 2$ . Substituting (39) into (36b), (36a), (38a) (38d) and using the fact that  $\mathcal{T}(x^{1/3}, [x_{\min}, x_{\max}])$  converges at a rate  $O(\Delta x^2)$  show that each of these terms converges at a rate of  $O(Da \Delta x^2)$ . Similarly, one can substitute (39) into (37c), (38c), and (38f) and use the fact that  $\mathcal{T}(x^{1/3}, [x_{\min}, x_{\max}])$  converges at a rate of  $O(\Delta x^2)$ , to show that each of these terms converges at a rate of  $O(Da \Delta x^2)$ .

It remains to determine the error associated with (37b), (38b), and (38e), so we turn our attention to (37b) and substitute (39) into (37b) to obtain

$$-\frac{D_r^{1/3} Da}{F_r 3^{1/3} \Gamma(2/3) (x_{\max} - x_{\min})} \left( \frac{d^1 B_1}{dt} + \frac{d^1 B_{12}}{dt} \right) (t) \int_{x_{\min}}^{x_{\max}} \int_0^x (x - \nu)^{1/3} - x^{1/2} \frac{d\nu}{\nu^{2/3}}, \tag{40}$$

where we have used the definition of our averaging operator (4). In writing (40), neglected higher-order terms which do not contribute to the leading-order spatial discretization error. Since the coefficient of the integral in (40) is a function of time alone, this coefficient does not contribute to the leading-order spatial discretization error and we neglect it in our analysis. Hence, to compute the spatial discretization error associated with (40), we calculate the error associated with applying the trapezoidal rule to the double integral

$$\int_{x_{\min}}^{x_{\max}} \int_0^x \left[ (x - v)^{1/3} - x^{1/3} \right] \frac{dv}{v^{2/3}} dx. \tag{41}$$

Treating the inner integral as a function of  $x$ , we define

$$f(x) = \int_0^x \left( (x - v)^{1/3} - x^{1/3} \right) v^{-2/3} dv, \tag{42}$$

whose closed form is given by

$$f(x) = \frac{x^{2/3}}{2} \left( \frac{2^{1/3} \sqrt{\pi} \Gamma\left(\frac{1}{3}\right)}{\Gamma\left(\frac{5}{6}\right)} - 6 \right). \tag{43}$$

Toward applying the trapezoidal rule to (41), we first note  $\mathcal{T}(f, [0, x_i])$  converges at a rate of  $O(\Delta x^{4/3})$ . This is seen by first rewriting (42) as

$$\int_0^{\Delta x} \left[ (x - v)^{1/3} - x^{1/3} \right] v^{-2/3} dv + \int_{\Delta x}^{x_i} \left[ (x - v)^{1/3} - x^{1/3} \right] v^{-2/3} dv. \tag{44}$$

The term on the right converges at a rate of  $O(\Delta x^2)$ , and the term on the left converges at a rate of  $O(\Delta x^{4/3})$ , which follows from expanding  $(x - v)^{1/3}$  about  $v = 0$ , and using the definition of the trapezoidal rule.

Applying the trapezoidal rule to (41) then gives

$$\begin{aligned} & Da^2 \int_{x_{\min}}^{x_{\max}} \int_0^x \left( (x - v)^{1/3} - x^{1/3} \right) v^{-2/3} dv dx \\ &= \frac{Da^2 \Delta x}{2} \mathcal{T}(f(x), [0, x_m]) + \sum_{i=m+1}^{M-1} Da^2 \Delta x \mathcal{T}(f(x), [0, x_i]) \\ &+ \frac{Da^2 \Delta x}{2} \mathcal{T}(f(x), [0, x_M]) + O(Da^2 \Delta x^2), \end{aligned} \tag{45}$$

where we have let  $x_{\min} = x_m = m \Delta x$ , and  $x_{\max} = x_M = M \Delta x$ . Since  $\mathcal{T}(f, [0, x_i])$  converges at a rate of  $O(\Delta x^{4/3})$ , the right-hand side of the above is

$$\begin{aligned} & \left( \frac{Da^2 \Delta x}{2} f(x_m) + O(Da^2 \Delta x^{7/3}) \right) + \sum_{i=m+1}^{M-1} \left( Da^2 \Delta x f(x_i) + O(Da^2 \Delta x^{7/3}) \right) \\ &+ \left( \frac{Da^2 \Delta x}{2} f(x_M) + O(Da^2 \Delta x^{7/3}) \right) + O(Da^2 \Delta x^2). \end{aligned} \tag{46}$$

To compute our results in Sect. 5, we took  $x_{\min} = 0.2$ ,  $x_{\max} = 0.8$ , in accordance with the literature [Edwards and Jackson \(2002\)](#). Hence, in the above sum there are

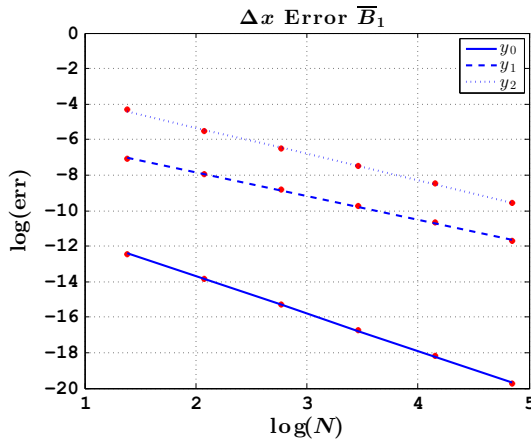


**Fig. 6** (Color figure online) Spatial convergence for  $\overline{B}_1$ ,  $Da = .01, 1, 10$ . The (solid) line  $y_0 = -2.10x - 9.49$  was fit to the error when  $Da = .01$ . The (dashed) line  $y_1 = -1.33x - 5.17$  was fit to the error when  $Da = 1$ . The (dotted) line  $y_2 = -1.48x - 2.36$  was fit to the error when  $Da = 10$ . All three lines have an  $R^2$  coefficient of  $R^2 = .99$ . The rate constants were taken equal to:  ${}_1K_d = 1, {}_2K_a = 1, {}_2K_d = 1, {}_1K_a = 1/2, {}_1K_d = 2, {}_2K_a = 2, \text{ and } {}_2K_d = 1/2$

approximately  $0.6N = 0.6\Delta x^{-1}$  terms on the order of  $O(Da^2 \Delta x^{7/3})$ , and the above sum reduces to

$$Da^2 \left( \frac{\Delta x}{2} f(x_m) + \sum_{i=m+1}^{M-1} \Delta x f(x_i) + \frac{\Delta x}{2} f(x_M) \right) + O(Da^2 \Delta x^{4/3}) + O(Da^2 \Delta x^{5/3}). \tag{47}$$

The dominant error in (47) is  $O(Da^2 \Delta x^{4/3})$ ; thus, the spatial discretization error associated with (37b) is  $O(Da^2 \Delta x^{4/3})$ . When measuring convergence, we used values of  $x_{\min} = .25, x_{\max} = .75$  to facilitate progressive grid refinement; however, it is clear that these values of  $x_{\min}$  and  $x_{\max}$  do not change our argument. A similar argument shows the spatial discretization error associated with the nonlinear terms (38b) and (38f) is  $O(Da^2 \Delta x^{4/3})$ .

We have depicted our spatial convergence measurements for  $\overline{B}_1$  in Fig. 6 and tabulated them in Table 1. To obtain these results, we first computed a reference solution, with  $\Delta x = \Delta t = 1/512$ . We then created a series of test solutions with mesh width  $\Delta x = 1/2^j$ , for  $j = 2, \dots, 7$ , keeping  $\Delta t = 1/512$  constant. Next, we computed  $\overline{B}$  by averaging our reference solution and test solutions at each time step with the trapezoidal rule as in (34). We then computed the error between each test solution and the reference solution by taking the maximum difference of the two over all time steps.

From our results, we see that our method converges at a rate of  $O(\Delta x^2)$  when  $Da \ll 1, O(\Delta x^{4/3})$  when  $Da = O(1)$ , and  $O(\Delta x^{3/2})$  when  $Da \gg 1$ . The reduction in convergence when  $Da$  increases from small to moderate may be attributed to the  $O(Da^2 \Delta x^{4/3})$  contributions from (37b), (38b), and (38e). There are two competing

**Table 1** Convergence results for the reacting species

	Da $\ll$ 1	Da = $O(1)$	Da $\gg$ 1
$\bar{B}_1$	$O(\Delta x^{2.09})$	$O(\Delta x^{1.33})$	$O(\Delta x^{1.48})$
$\bar{B}_{12}$	$O(\Delta x^{2.04})$	$O(\Delta x^{1.42})$	$O(\Delta x^{1.53})$
$\bar{B}_2$	$O(\Delta x^{2.09})$	$O(\Delta x^{1.33})$	$O(\Delta x^{1.46})$

Here Da = .01, 1, 10

magnitudes of error in (35a): one of  $O(Da \Delta x^2)$  (from terms (36b), (36a), (37c), (38a), (38c), (38d), and (38f)) and one of  $O(Da^2 \Delta x^{4/3})$  (from the integral terms (37b), (38b), and (38e)). When  $Da^2 \Delta x^{4/3} < Da \Delta x^2$ , or  $Da < \Delta x^{2/3}$ , the former is larger. Conversely, when  $\Delta x^{2/3} < Da$  the latter is larger.

When  $Da \gg 1$ , the bound state evolves on a longer timescale of the form (Edwards 1999)

$$t_w = t/Da. \tag{48}$$

In this case, the characteristic timescale for reaction for reaction is much faster than the characteristic timescale for transport into the surface, and one typically refers to  $Da \gg 1$  as the *transport-limited* regime. Substituting (48) into (7), (9), one may find the leading-order approximation to the resulting system for  $Da \gg 1$  by neglecting the left-hand side of (7a)–(7c). Doing so one finds that even a leading-order approximation to (7a)–(7c) is nonlinear, rendering any error estimates in the transport-limited regime beyond reach. Nonetheless, our results in Fig. 6 and Table 1 show that convergence is not an issue when  $Da \gg 1$ .

### 4.2.2 Temporal Convergence

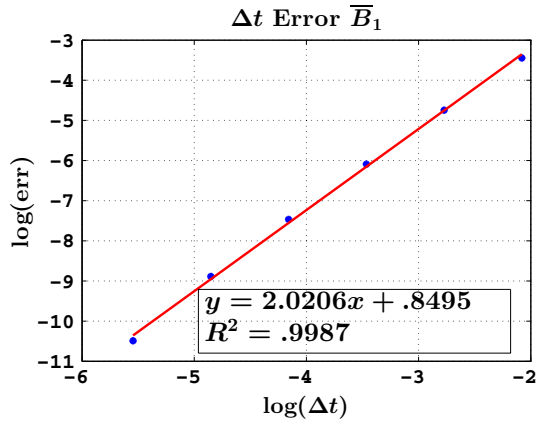
Since our time stepping method (32b) is analogous to a second-order Adams–Bashforth formula, we expect our method to achieve second-order accuracy in time. Figure 7 shows that this is indeed the case when  $Da = .01$ , and the rate constants are  ${}_1K_d = 1$ ,  ${}_2K_a = 1$ ,  ${}_2K_d = 1$ ,  ${}_1K_a = 1/2$ ,  ${}_1K_d = 2$ ,  ${}_2K_a = 2$ , and  ${}_2K_d = 1/2$  (as in Sect. 4.2.1 when measuring spatial convergence). Temporal convergence was measured in an analogous manner to spatial convergence.

However, we note that measuring temporal convergence when  $Da = O(1)$  is computationally prohibitive, since spatial convergence is  $O(Da^2 \Delta x^{4/3})$  in this case, so in order for the spatial and temporal errors to balance one must have  $O(Da^2 \Delta x^{4/3}) = O(\Delta t^2)$  or  $\Delta x = \Delta t^{3/2}$ . Nonetheless, our results from Sect. 5 demonstrate that our finite difference approximation agrees with our ERC approximation for a wide parameter range, so we are not concerned with temporal convergence of our method when  $Da = O(1)$  or larger.

### 4.2.3 Stability Remarks

We now make brief remarks concerning the stability of our method. Recall from Sect. 4.1, we first determine the value of  $B_i(x, t)$  upstream at  $x = 0$  and iteratively

**Fig. 7** (Color figure online) Temporal convergence when  $Da = .01$ , and  ${}_1K_d = 1$ ,  ${}_2K_a = 1$ ,  ${}_2K_d = 1$ ,  ${}_1K_a = 1/2$ ,  ${}_2K_d = 2$ ,  ${}_1K_a = 2$ , and  ${}_2K_d = 1/2$ . As expected, our method converges at a rate on the order of  $O(\Delta t^2)$



march our way downstream to  $x = 1$  at each time step. Therefore, we expect any instabilities at  $x = 0$  to propagate downstream. Requiring that there are no instabilities at  $x = 0$  is equivalent to asking that our time stepping method (32b) is stable for the ODE system found by replacing  $C_1(x, 0, t)$  and  $C_2(x, 0, t)$  with the constant function 1 in (7). Though we do not have precise stability estimates for this system, numerical experimentation has shown that our time steps need to be sufficiently small in order to ensure that our numerical approximation is well behaved.

### 5 Effective Rate Constant Approximation Verification

With our numerical method in hand, we are now in a position to verify the accuracy of our ERC approximations (22) and (23). We tested the accuracy of our ERC equations when  $Da = 0.1$ , and  $Da = 0.45$ ; the results are shown in Fig. 8 and Tables 2 and 3.

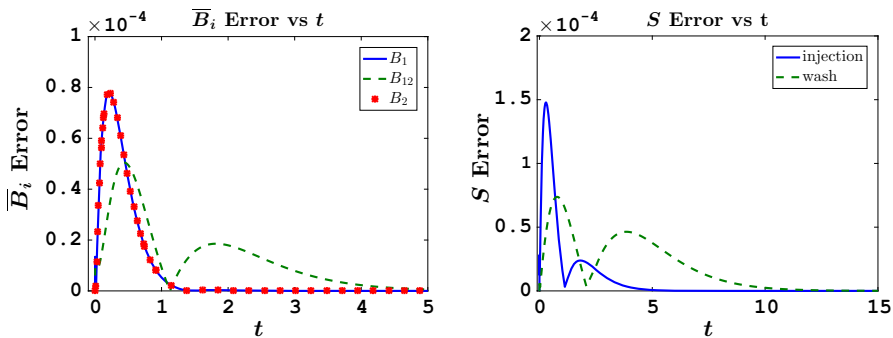


**Fig. 8** (Color figure online) *Left* error in the reacting species concentrations during the injection phase, computed by taking the absolute difference between the solution of our ERC equation (22) and our finite difference solution. We have taken  $Da = 0.1$ , and all of the rate constants equal to 1. Since the errors for  $\bar{B}_1$  and  $\bar{B}_2$  are identical, we plotted the error for  $\bar{B}_2$  on a coarser mesh; however, the errors for all three species were computed on precisely the same time steps. *Right* the error in the sensogram signal during both phases, when  $Da = .1$  and all of the rate constants are taken equal to 1

**Table 2** Maximum difference between our injection phase ERC approximation (22) and our finite difference solution

	$\bar{B}_1$	$\bar{B}_{12}$	$\bar{B}_2$	$\mathcal{S}$
Da = .1	$7.81 \times 10^{-5}$	$5.04 \times 10^{-5}$	$7.81 \times 10^{-5}$	$1.47 \times 10^{-4}$
Da = .45	$1.00 \times 10^{-3}$	$6.93 \times 10^{-4}$	$1.00 \times 10^{-3}$	$2.00 \times 10^{-3}$

All rate constants take equal to 1 in both cases

**Table 3** Maximum difference between our wash phase ERC approximation (22) and our finite difference solution

	$\bar{B}_1$	$\bar{B}_{12}$	$\bar{B}_2$	$\mathcal{S}$
Da = .1	$3.578 \times 10^{-5}$	$3.40 \times 10^{-5}$	$3.58 \times 10^{-5}$	$7.37 \times 10^{-5}$
Da = .45	$4.33 \times 10^{-4}$	$4.62 \times 10^{-4}$	$4.33 \times 10^{-4}$	$9.45 \times 10^{-4}$

All rate constants take equal to 1 in both cases

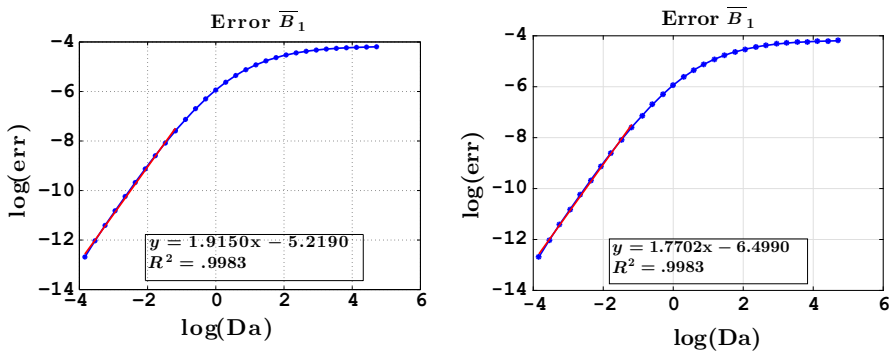


**Fig. 9** (Color figure online) *Left* absolute error in our injection phase approximation (22) over all time, for different values of Da. *Right* absolute error in our wash phase approximation (23) over all time, for different values of Da. *Both* the rate constants were taken equal to:  ${}_1K_d = 1/2$ ,  ${}_2K_a = 1$ ,  ${}_2K_d = 1$ ,  ${}_1^2K_a = 1$ ,  ${}_1^2K_d = 2$ ,  ${}_1K_a = 2$ , and  ${}_2^1K_d = 1/2$ . Similar results hold for  $B_{12}$ , and  $B_2$

From these results, it is evident that our ERC equations accurately characterize  $\bar{\mathbf{B}}$  and the sensogram reading (6) not only for small Da, but for moderate Da as well. Motivated by Edwards and Jackson (2002), we ran a series of simulations for different values of Da, ranging from  $Da \approx 0.02$  to  $Da = 150$ . We measured the maximum absolute error for each value of Da and created the curves shown in Fig. 9. The error starts off small as expected and increases at rates which compares favorably with our  $O(Da^2)$  prediction, and finally reaches an asymptote corresponding to roughly two percent absolute error. Thus, although our ERC approximations (22) and (23) are formally valid for only small values of Da, their solutions agree with our finite difference approximation for moderate and large values of Da.

## 6 Conclusions

Scientists are attempting to determine whether the polymerase  $\eta$  and PCNA complex (denoted  $EL_2$  throughout) which results from DNA translesion synthesis forms through direct binding (2a), or through a catalysis-type ligand switching process (2b). Since fluorescent labeling techniques may modify protein behavior, label-free optical biosensor experiments are used. Interpreting experimental data relies on a mathematical model, and modeling multiple-component biosensor experiments results in a complicated and unwieldy set of equations. We have shown that in experimentally relevant limits this model reduces to a much simpler set of ODEs (our ERC equations), which can be used to fit rate constants using biosensor data. In contrast with the standard well-stirred kinetics approximation, our ERC equations accurately characterize binding when mass transport effects are significant. This renders our ERC equations a flexible tool for estimating the rate constants in (2). In turn, estimates for the rate constants in (2) will reveal whether the polymerase  $\eta$  and PCNA complex forms via direct binding (2a) or the catalysis-type ligand switching process (2b).

Furthermore, the consideration of both direct binding (2a) and the ligand switching process (2b) has several mathematical and physical consequences. First, due to the form of (2), the species are directly coupled through the kinetics equations. This is true even in the well-stirred limit in which  $Da \rightarrow 0$  and (9) reduces to  $C_1(x, 0, t) = C_2(x, 0, t) = 1$ . However, transport effects manifested in (9) nonlinearly couple the reacting species. So we see in Fig. 4 that there is a more pronounced depletion region in  $B_{12}$  than in either of the other two species. Physically, this is a consequence of the fact that either  $EL_1$  or  $EL_2$  must be present in order for  $EL_1L_2$  to form; thus, the latter is affected by depletion of the former two species. Additionally, the multiple-component reactions (2) alter the form of the sensogram reading to the lumped signal (6), thereby complicating parameter estimation.

In addition to establishing a firm foundation for studying the inverse problem of estimating the rate constants in (2), the present work also opens the door for future work on modeling and simulating multiple-component biosensor experiments. This includes considering other physical effects like cross-diffusion or steric hindrance and comparing the finite difference method described herein to the method of lines algorithm discussed in Zumburum (2013).

## Appendix: Parameter Values

Parameter values from the literature are tabulated.

The variables  $W$ ,  $Q$  represent the dimensional width and flow rate; the other dimensional variables are as in Sect. 2. The flow rate is related to the velocity through the formula (Edwards 2011)

$$V = \frac{6Q}{WH}. \quad (\text{A.1})$$

Using the dimensional values above, we calculated the following *extremal bounds* on the dimensionless variables.

Here  $\epsilon = H/L$  is the aspect ratio, and  $Re = VH^2/(\nu L)$  is the appropriate Reynolds number associated with our system.

The authors wish to emphasize that the bounds in Table 5 are naïve extremal bounds calculated by using minimum and maximum values for the dimensional parameters in Table 4. In particular, the values for the dimensionless rate constants in Table 5 are not estimates of their true values; they are minimum and maximum values calculated using combinations of *extremal values* for the parameters in Table 5. A large variation in the dimensionless rate constants is highly unlikely, since this scenario corresponds to one in which one of the association rate constants is very large, and another association rate constant very small. We would also like to note that a large variation in some of

**Table 4** Dimensional parameter ranges, taken from references de la Torre et al. (2000), Gen (2013), Rich et al. (2008), and Yarmush et al. (1996)

Parameter	Rich et al. (2008)	Yarmush	BIAcore T200	Torre
$k_a [10^8 \text{ cm}^3/(\text{mol s})]$	$10^{-4} - 10^{-2}$	$.5 - 5 \times 10$	$10^{-5} - 3 \times 10$	
$k_d (10^{-3} \text{ s}^{-1})$	1	8.9	$10^{-2} - 10^3$	
$D_1 (10^{-7} \text{ cm}^2/\text{s})$				4.0
$D_2 (10^{-7} \text{ cm}^2/\text{s})$				6.88
$H (1 \text{ cm})$	.05	.04		
$L (1 \text{ cm})$	2			
$W (1 \text{ cm})$	1.3			
$R_T (10^{-12} \text{ mol}/\text{cm}^2)$	$1.11 \times 10^{-1} - 2.33 \times 10^1$	2.5–4		
$Q (1 \mu\text{L}/\text{min})$	100–1500		1–100	
$V (1 \text{ cm}/\text{s})$	.153–2.88	.36–.6	.001–1.92	
$C_{i,u} (10^{-11} \text{ mol}/\text{cm}^3)$	$2.96 \times 10^{-1} - 2 \times 10^1$			

**Table 5** Dimensionless parameters

Parameter	Bound
$\epsilon$	0.02–0.025
Re	$8.00 \times 10^{-5} - 0.36$
Pe	0.12–523.26
Da	$9.29 \times 10^{-8} - 1.49 \times 10^3$
${}_2K_a$	$2.96 \times 10^{-9} - 3.38 \times 10^8$
$\frac{1}{2}K_a$	$2.96 \times 10^{-9} - 3.38 \times 10^8$
$\frac{2}{1}K_a$	$2 \times 10^{-7} - 5 \times 10^6$
$iK_d$	$1 \times 10^{-5} - 3.38 \times 10^8$
$\frac{j}{i}K_d$	$1 \times 10^{-5} - 3.38 \times 10^8$
$D_r$	0.58
$F_r$	0.01–39.28

the parameters, such as the kinetic rate constants or  $Da$ , would necessitate very small values for either or both of  $\Delta t$  and  $\Delta x$  in our numerical method.

Furthermore, one may be concerned about the upper bound on the Reynolds number, the lower bound on the Péclet number, and the upper bound on the Damköhler number. All of these extremal bounds were calculated using a flow rate of  $1 \mu\text{L}/\text{min}$ —the slowest flow rate possible on the BIAcore T200 (Gen 2013). Even with the fastest reactions, one can still design experiments to minimize transport effects by increasing the flow rate  $Q$  (thus the velocity), decreasing the initial empty receptor concentration  $R_T$ , and decreasing the ligand inflow concentrations  $C_{1,u}$  and  $C_{2,u}$ . In the case of the fastest reaction  ${}_1k_a = 3 \times 10^9 \text{ cm}^3/(\text{mol s})$ , we can take:  $Q = 390 \mu\text{L}/\text{min}$ ,  $V = .75 \text{ cm/s}$ ,  $R_T = 7.76 \times 10^{-13} \text{ mol}/\text{cm}^2$ ,  $C_{1,u} = C_{2,u} = 2.96 \times 10^{-12} \text{ mol}/\text{cm}^3$ . These choices yield the dimensionless parameters  $Re = 0.09$ ,  $Pe = 136.26$ ,  $Da = 5.16$ ; these values are perfectly in line with our analysis and the validity of our ERC equations.

## References

- BIAcore T200 data file (2013) General electric life sciences, GE Healthcare bio-sciences AB, Björkgatan 30, 751 84 Uppsala, Sweden, April 2013
- de la Torre JG, Huertas ML, Carrasco B (2000) Calculation of hydrodynamic properties of globular proteins from their atomic-level structure. *Biophys J* 78(2):719–730
- Edwards DA (1999) Estimating rate constants in a convection-diffusion system with a boundary reaction. *IMA J Appl Math* 63(1):89–112
- Edwards DA (2000) Biochemical reactions on helical structures. *SIAM J Appl Math* 42(4):1425–1446
- Edwards DA (2001) The effect of a receptor layer on the measurement of rate constants. *Bull Math Biol* 63(2):301–327
- Edwards DA (2006) Convection effects in the BIAcore dextran layer: surface reaction model. *Bull Math Biol* 68:627–654
- Edwards DA (2011) Transport effects on surface reaction arrays: biosensor applications. *Math Biosci* 230(1):12–22
- Edwards DA, Evans RM, Li W (2017) Measuring kinetic rate constants of multiple-component reactions with optical biosensors. *Anal Biochem* 533:41–47
- Edwards DA, Jackson S (2002) Testing the validity of the effective rate constant approximation for surface reaction with transport. *Appl Math Lett* 15(5):547–552
- Edwards DA, Goldstein B, Cohen DS (1999) Transport effects on surface–volume biological reactions. *J Math Biol* 39(6):533–561
- Friedberg EC (2005) Suffering in silence: the tolerance of DNA damage. *Nat Rev Mol Cell Biol* 6(12):943–953
- Karlsson R, Fält A (1997) Experimental design for kinetic analysis of protein-protein interactions with surface plasmon resonance biosensors. *J Immunol Methods* 200(1):121–133
- Lebedev K, Mafé S, Stroeve P (2006) Convection, diffusion, and reaction in a surface-based biosensor: modeling of cooperativity and binding site competition and in the hydrogel. *J Colloid Interface Sci* 296:527–537
- Lehmann AR, Niimi A, Ogi T, Brown S, Sabbioneda S, Wing JF, Kannouche PL, Green CM (2007) Translesion synthesis: Y-family polymerases and the polymerase switch. *DNA Repair* 6(7):891–899
- Morton TA, Myszka DG, Chaiken IM (1995) Interpreting complex binding kinetics from optical biosensors: a comparison of analysis by linearization, the integrated rate equation, and numerical integration. *Anal Biochem* 227(1):176–185
- Nie Q, Zhang Y-T, Zhao R (2006) Efficient semi-implicit schemes for stiff systems. *J Comput Phys* 214(2):521–537
- Plosky BS, Woodgate R (2004) Switching from high-fidelity replicases to low-fidelity lesion-bypass polymerases. *Curr Opin Genet Dev* 14(2):113–119

- Rich RL, Myszka DG (2009) Extracting kinetic rate constants from binding responses. In: Cooper MA (ed) Label-free biosensors. Cambridge University Press, Cambridge
- Rich RL, Cannon MJ, Jenkins J, Pandian P, Sundaram S, Magyar R, Brockman J, Lambert J, Myszka DG (2008) Extracting kinetic rate constants from surface plasmon resonance array systems. *Anal Biochem* 373(1):112–120
- Yarmush ML, Patankar DB, Yarmush DM (1996) An analysis of transport resistances in the operation of BIAcore; implications for kinetic studies of biospecific interactions. *Mol Immunol* 33(15):1203–1214
- Zhuang Z, Johnson RE, Haracska L, Prakash L, Prakash S, Benkovic SJ (2008) Regulation of polymerase exchange between pol $\eta$  and pol $\delta$  by monoubiquitination of pcna and the movement of dna polymerase holoenzyme. *Proc Natl Acad Sci* 105(14):5361–5366
- Zumbrum M (2013) Extensions for a surface–volume reaction model with application to optical biosensors. Ph.D. thesis, University of Delaware
- Zumbrum M, Edwards DA (2014) Multiple surface reactions in arrays with applications to optical biosensors. *Bull Math Biol* 76(7):1783–1808
- Zumbrum M, Edwards DA (2015) Conformal mapping in optical biosensor applications. *J Math Biol* 71(3):533–550